Supporting Information

Fabrication of Cu-MOFs derived nanofiber membranes for efficient removal of environmental pollutants

Wen-Ze Li,[a] Fu-Yu Guo,[a] Sheng Qu,[b*] Jing Li,[c] Yi Ru,[d] Xiao-Sa Zhang,[a] Yu Liu,[a] and Jian Luan[a*]

[a] *College of Science, Shenyang University of Chemical Technology, Shenyang, 110142, P. R. China*

[b] *Department of Radiology, The 966th Hospital of The PLA Joint Logistic Support Force, Dandong, 118000, P. R. China*

[c] *College of Chemistry, Liaoning University, Shenyang, 110036, P. R. China*

[d] *School of Science, Xi'an Jiaotong-Liverpool University, Suzhou, 215123, P. R. China*

E-mails: jluan@syuct.edu.cn (Jian Luan); radiology7311@sina.com (Sheng Qu)

S1.1. Materials and methods.

N,*N*′-bis(pyridin-3-yl)cyclohexane-1,4-dicarboxamide (3-bcda) and *N*,*N*′-bis(3-pyridyl)adipamide (3-bpaa) were prepared by the method outlined in the literature.[S1] All the additional chemicals, solvents and gases used in this synthesis were purchased from commercial suppliers and used directly from the packaging.

S1.2 X-ray Crystallography.

Crystallographic data for **Cu-MOF-1** and **Cu-MOF-2** were collected by ω and θ scanning modes on the Bruker SMART APEX II with Cu Kα (λ = 0.71073 Å). All structures were solved by direct methods and refined on F^2 by full matrix least squares using SHELXTL software package.[S2] Table S1 provided an overview of **Cu-MOF-1** and **Cu-MOF-2** crystal characterization, data collection, and refinement results. Tables S2 and S3 provided options for bonding angles and bonding distances.

S1.3 Characterization.

Elemental analysis of C, H, and N was determined using a PerkinElmer 240C elemental analyzer. Fourier transform infrared (FTIR) spectra of KBr particles in the range of 4000–500 cm^{-1} were recorded on a Varian 640-IR spectrometer. The thermal

stability of Cu-MOFs were determined on a thermogravimetric (TG) analyzer (Netzsch 449c). Powder X-ray diffraction (PXRD) patterns were performed by using a Rigaku diffractometer. Scanning electron microscopy (SEM) was used to analyze and characterize the shape and structure of the materials (Nova Nano SEM 430). An Escalab 250 device with an Al Kα radiation source was used to carry out X-ray photoelectron spectroscopy (XPS) characterization. Ultraviolet−visible (UV-vis) absorption spectra were obtained by using an SP-1900 UV-vis spectrophotometer. Solid UV was measured by a Cary 5000 UV-visible near-infrared spectrophotometer.

S1.4 Photocatalytic degradation of dyes.

The adsorption and photocatalytic activities of **Cu-MOF-X@PAN**, **Cu-1-X@PAN** and **Cu-2-X@PAN** were investigated under dark and UV-visible irradiation with three known concentrations of azo dye aqueous solutions of methyl orange (MO), Congo red (CR) and crystal violet (GV). In a typical photocatalytic experiment, 5 mg of material was added to 50 mL of dye aqueous solution (MO, CR, GV are all 10 mg L^{-1}). Before using a UV light source, the suspension was continuously stirred at room temperature in the dark for 2 h to achieve a balance of adsorption and desorption between the dye and the system. Finally, the secondary dye concentrations (λ_{max}(MO) = 465 nm, λ_{max}(CR) = 497 nm, and λ_{max}(GV) = 589 nm) were determined using the equations obtained from the calibration curve with the UV-vis spectrophotometer. After the adsorption equilibrium between the five dyes and the system was reached, a 20 W high-pressure mercury lamp was used as the UV-vis light source to irradiate the catalyst and the suspension of the five dyes. **Cu-1-X@PAN** and **Cu-2-X@PAN** were separately recovered from the aqueous solution by centrifugation following each adsorption cycle. Anhydrous ethanol was used to wash and dry the recovered fiber films at 60 °C. The synthesized **Cu-1-X@PAN** and **Cu-2-X@PAN** were recovered and utilized again in dye adsorption under comparable conditions in order to test their reusability.

The absorbance changes during the observed reaction time intervals in the bisection

samples were monitored by an ultraviolet-visible spectrophotometer. The maximum absorbance measured at different reaction times was converted into the degradation rate of five dyes and expressed as the degradation rate = $(C_0 – C_T)/C_0 \times 100\%$.

S1.5 Experiment of dye photocatalysis mechanism.

Three different types of free radical trapping agents were used to perform photocatalytic quenching experiments, and the photocatalytic degradation mechanism of the prepared materials was evaluated by the degradation of GV aqueous solution under dark and ultraviolet irradiation. After adding 5 mg of material to 50 mL GV solution (10 mg L^{-1}), three trapping agents were added separately. Stir the solution continuously in the dark for at least 2 h, and then use a UV light source to help the adsorption-desorption balance between the dye and the system. Using this system, the five dyes were able to achieve a balance between adsorption and desorption. Next, a 20 W high-pressure mercury lamp was used as a UV light source to irradiate the catalyst solution and five dyes. Changes in absorbance were tracked using a UV-Vis spectrophotometer during the time period during which the reaction in the isometric sample was observed. Next, the catalyst solution and five dyes were exposed to UV radiation using a 20 W high-pressure mercury lamp. Using a UV-Vis spectrophotometer, changes in absorbance were monitored throughout the time that the reaction in the isometric sample was detected.

Supporting Information

Table S1 Crystallographic data for **Cu-MOF-1** and **Cu-MOF-2**.

MOF	**Cu-MOF-1**	**Cu-MOF-2**
CCDC number	2377225	2377226
Empirical formula	$C_{90}H_{86}Cu_3N_{12}O_{22}$	$C_{40}H_{32}Cu_3N_4O_{12}$
Formula weight	1878.33	951.32
Crystal system	Triclinic	Monoclinic
Space group	*P*–1	*P*21/*n*
a (Å)	9.119(2)	15.6620(13)
b (Å)	15.178(3)	6.5261(5)
c (Å)	16.895(3)	19.8923(15)
α (°)	95.132(6)	90
β (°)	93.141(7)	106.472(3)
γ (°)	99.555(7)	90
V (Å^3)	2290.8(8)	1949.8(3)
Z	1	2
D_c (g cm^{-3})	1.362	1.620
Crystal size (mm^3)	0.16 × 0.14 × 0.12	0.15 × 0.13 × 0.11
R_{int}	0.0649	0.0737
GOF	1.062	1.097
R_1[a] [$I > 2\sigma(I)$]	0.1079	0.0416
wR_2[b] (all data)	0.3969	0.1183

[a] $R_1 = \sum||F_o| - |F_c||/\sum|F_o|$, [b] $wR_2 = \sum [w (F_o^2 - F_c^2)^2]/\sum [w (F_o^2)^2]^{1/2}$.

Table S2 Selected bond distances (Å) and angles (°) for **Cu-MOF-1**.

Cu(1)–O(1)	1.916(4)	N(2)–Cu(1)#3	2.042(5)
Cu(1)–O(5)	1.969(4)	O(5)–Cu(1)–N(2)#1	88.81(18)
Cu(1)–N(1)	2.023(5)	N(1)–Cu(1)–N(2)#1	166.7(2)
Cu(1)–N(2)#1	2.042(5)	O(1)–Cu(1)–O(1W)	87.4(2)
Cu(1)–O(1W)	2.426(5)	O(5)–Cu(1)–O(1W)	89.44(19)
Cu(2)–O(3)	1.966(4)	N(1)–Cu(1)–O(1W)	98.2(2)
Cu(2)–O(3)#2	1.966(4)	N(2)#1–Cu(1)–O(1W)	94.7(2)
Cu(2)–N(5)	1.999(6)	O(3)–Cu(2)–O(3)#2	179.999(3)
Cu(2)–N(5)#2	1.999(6)	O(3)–Cu(2)–N (5)	88.9(2)
O(1)–Cu(1)–O(5)	176.4(2)	O(3)#2–Cu(2)–N(5)	91.1(2)
O(1)–Cu(1)–N(1)	94.0(2)	O(3)–Cu(2)–N(5)#2	91.1(2)
O(5)–Cu(1)–N(1)	88.10(19)	O(3)#2–Cu(2)–N(5)#2	88.9(2)
O(1)–Cu(1)–N(2)#1	89.7(2)	N(5)–Cu(2)–N(5)#2	179.999(3)

Symmetry codes: #1 x, y, $z + 1$; #2 $–x + 1$, $–y + 2$, $–z + 2$.

Table S3 Selected bond distances (Å) and angles (°) for **Cu-MOF-2**.

Cu(1)–O(6)	1.908(2)	O(6)#1–Cu(1)–O(1)	86.82(10)
Cu(1)–O(6)#1	1.908(2)	O(1)#1–Cu(1)–O(1)	179.998(1)
Cu(1)–O(1)#1	1.926(2)	O(3)–Cu(2)–O(2)	174.65(11)
Cu(1)–O(1)	1.926(2)	O(3)–Cu(2)–O(6)	89.83(9)
N(1)–Cu(2)	2.013(3)	O(2)–Cu(2)–O(6)	91.35(9)
Cu(2)–O(3)	1.959(2)	O(3)–Cu(2)–N(1)	90.92(11)
Cu(2)–O(2)	1.960(2)	O(2)–Cu(2)–N(1)	87.57(10)
Cu(2)–O(6)	1.964(2)	O(6)–Cu(2)–N(1)	176.12(11)
Cu(2)–O(6)#2	2.325(2)	O(3)–Cu(2)–O(6)#2	97.88(9)
O(6)–Cu(1)–O(6)#1	180.0	O(2)–Cu(2)–O(6)#2	87.41(9)
O(6)–Cu(1)–O(1)#1	86.82(10)	O(6)–Cu(2)–O(6)#2	86.34(8)
O(6)#1–Cu(1)–O(1)#1	93.18(10)	N(1)–Cu(2)–O(6)#2	97.33(10)
O(6)–Cu(1)–O(1)	93.18(10)		

Symmetry codes: #1 $-x, -y, -z + 1$; #2 $-x, -y + 1, -z + 1$.

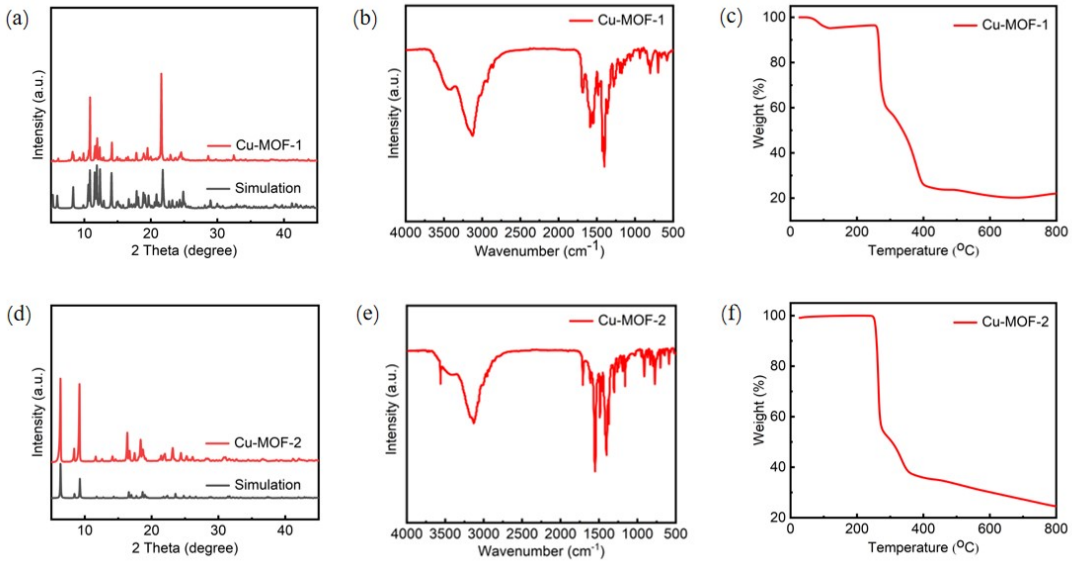

Fig. S1 PXRD patterns (a), FTIR spectra (b), TG curve (c) of **Cu-MOF-1**. PXRD patterns (d), FTIR spectra (e), TG curve (f) of **Cu-MOF-2**.

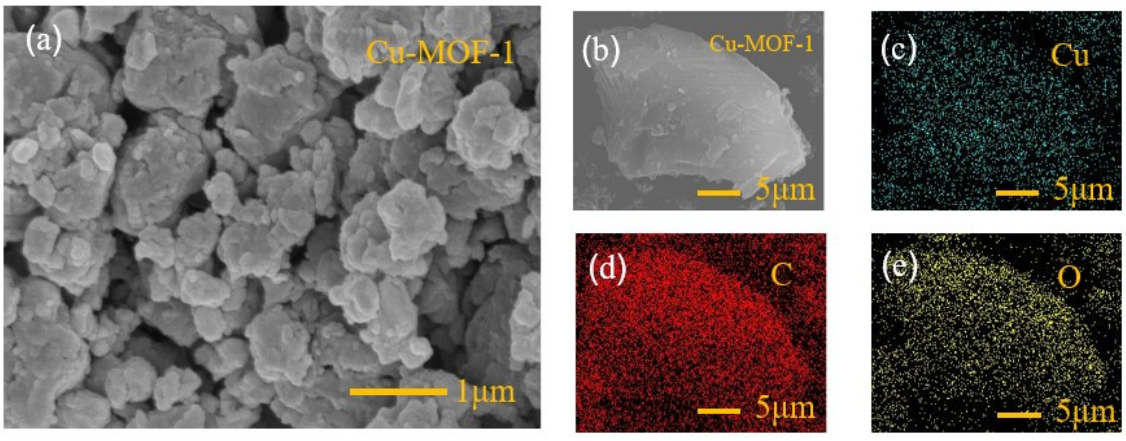

Fig. S2 (a) SEM image of **Cu-MOF-1**. (b–e) EDX images of **Cu-MOF-1**.

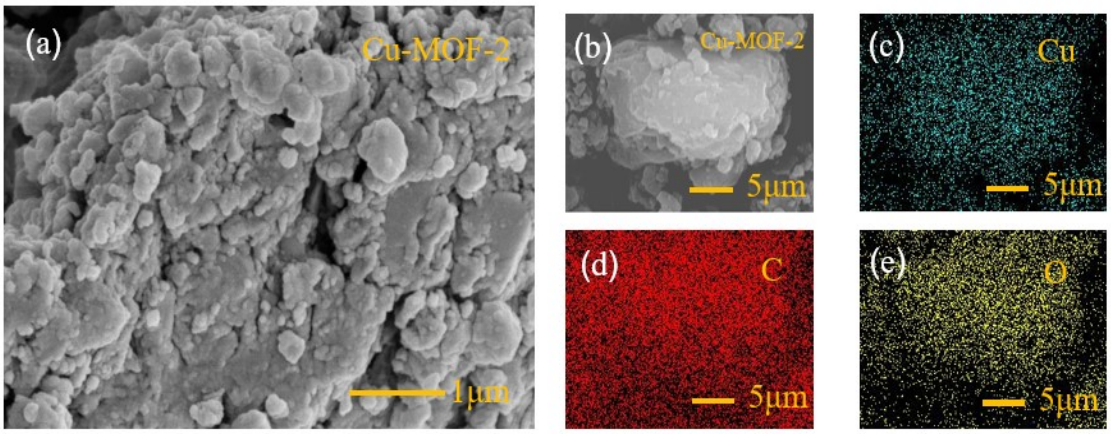

Fig. S3 (a) SEM image of **Cu-MOF-2**. (b–e) EDX images of **Cu-MOF-2**.

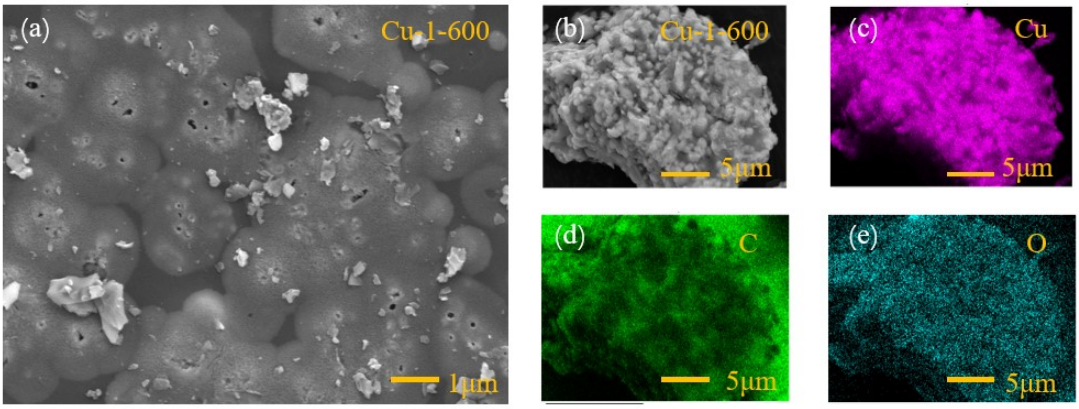

Fig. S4 (a) SEM image of **Cu-1-600**. (b–e) EDX images of **Cu-1-600**.

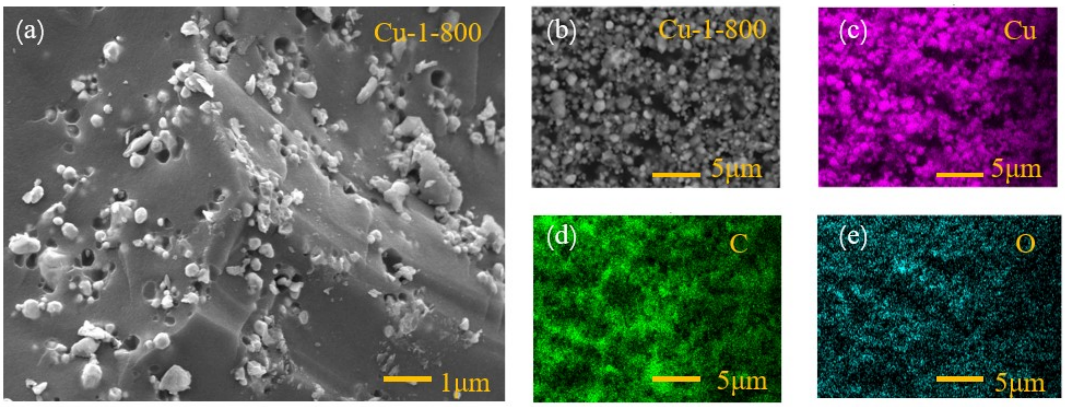

Fig. S5 (a) SEM image of **Cu-1-800**. (b–e) EDX images of **Cu-1-800**.

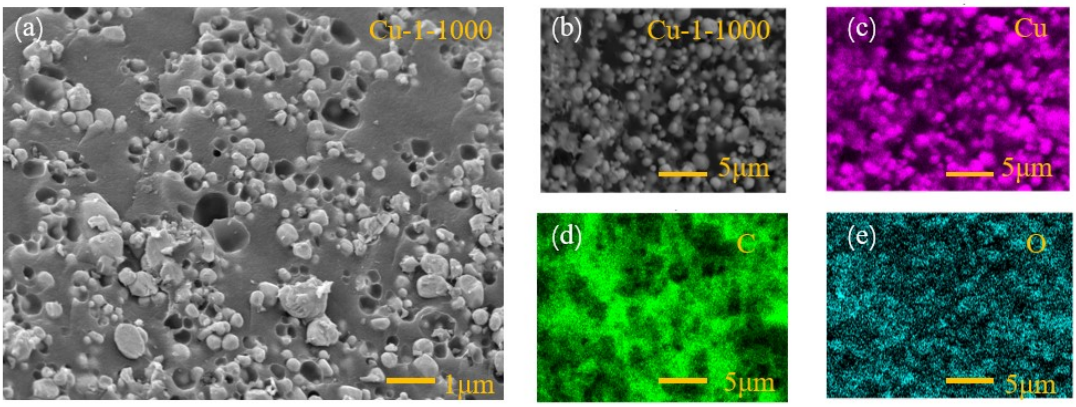

Fig. S6 (a) SEM image of **Cu-1-1000**. (b–e) EDX images of **Cu-1-1000**.

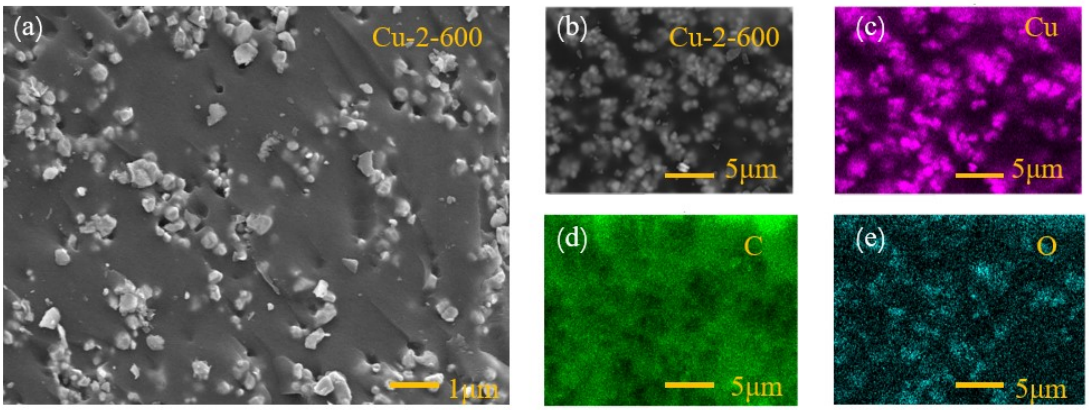

Fig. S7 (a) SEM image of **Cu-2-600**. (b–e) EDX images of **Cu-2-600**.

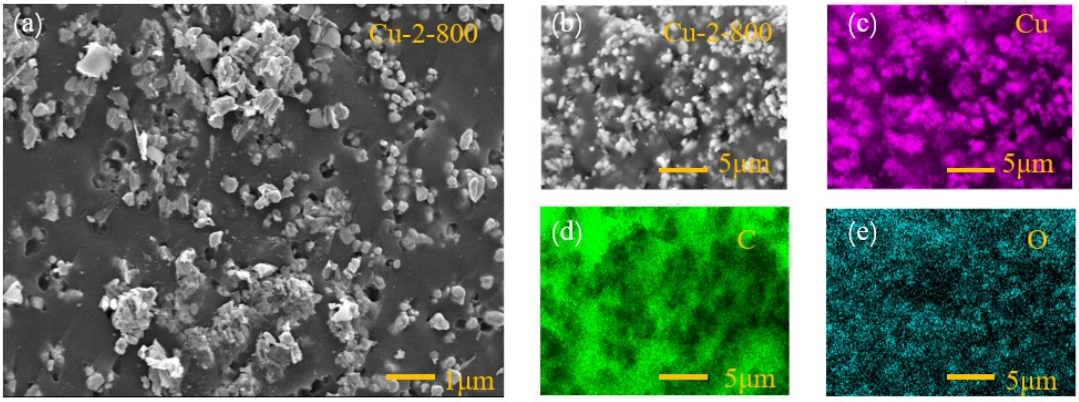

Fig. S8 (a) SEM image of **Cu-2-800**. (b–e) EDX images of **Cu-2-800**.

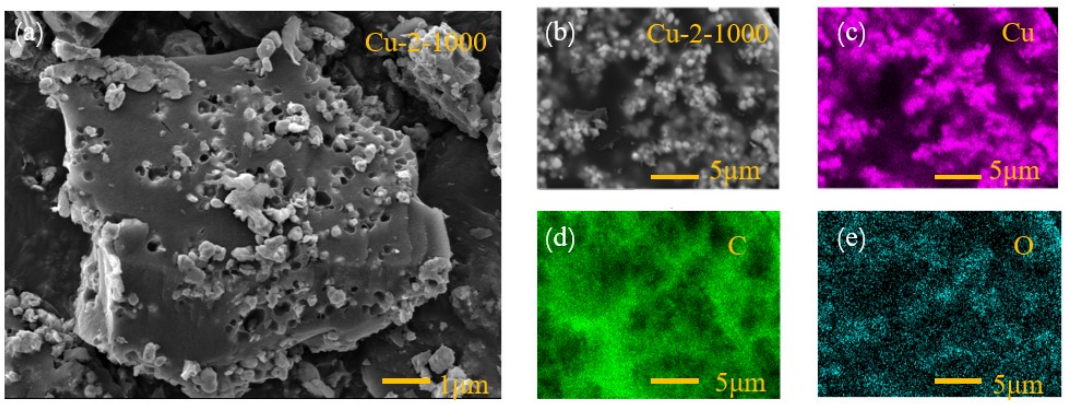

Fig. S9 (a) SEM image of **Cu-2-1000**. (b–e) EDX images of **Cu-2-1000**.

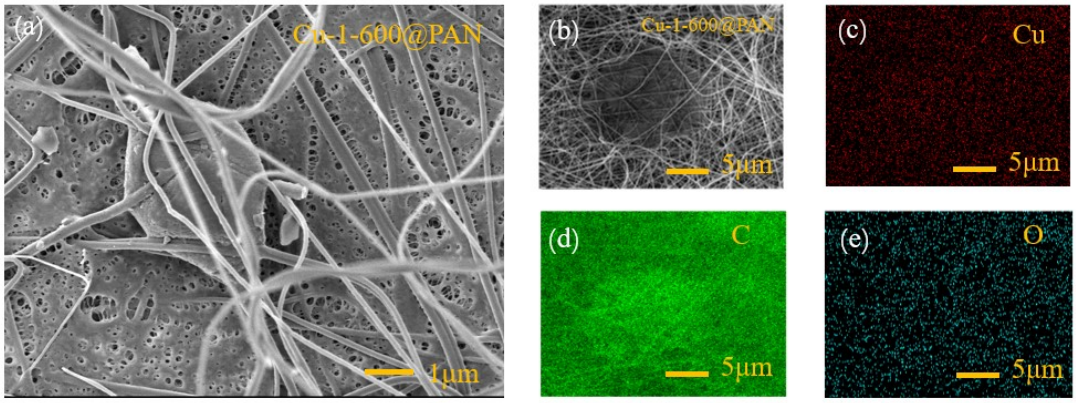

Fig. S10 (a) SEM image of **Cu-1-600@PAN**. (b–e) EDX images of **Cu-1-600@PAN**.

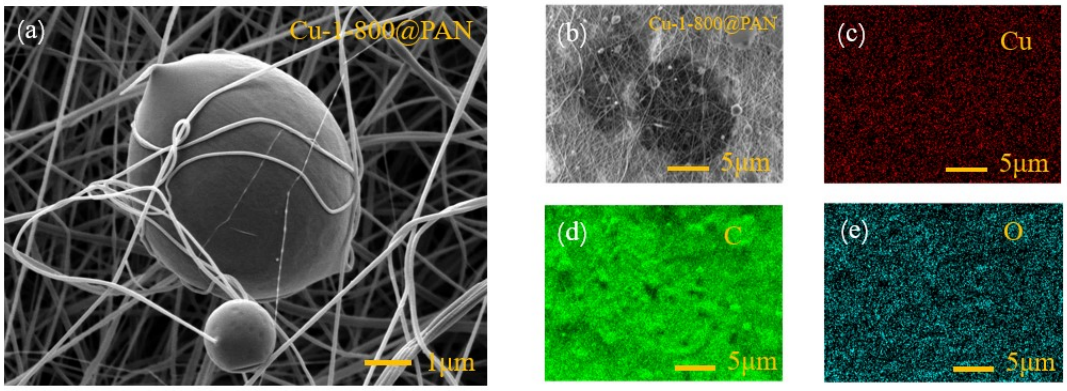

Fig. S11 (a) SEM image of **Cu-1-800@PAN**. (b–e) EDX images of **Cu-1-800@PAN**.

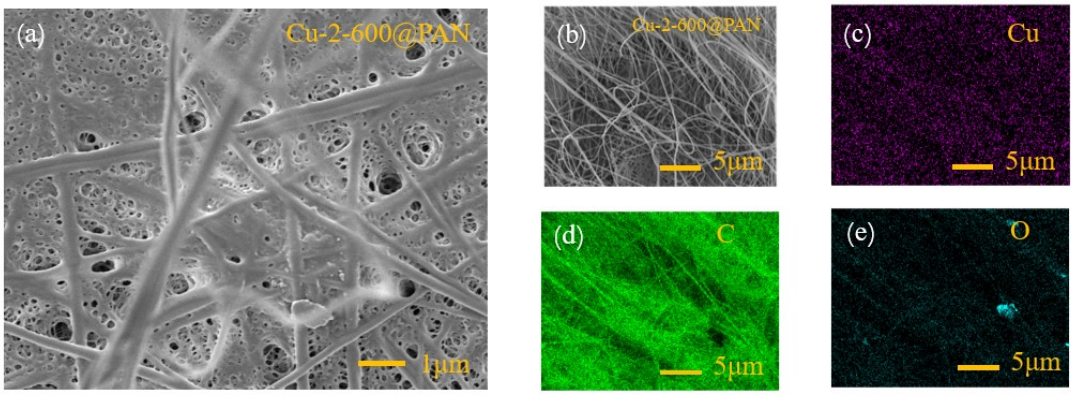

Fig. S12 (a) SEM image of **Cu-2-600@PAN**. (b–e) EDX images of **Cu-2-600@PAN**.

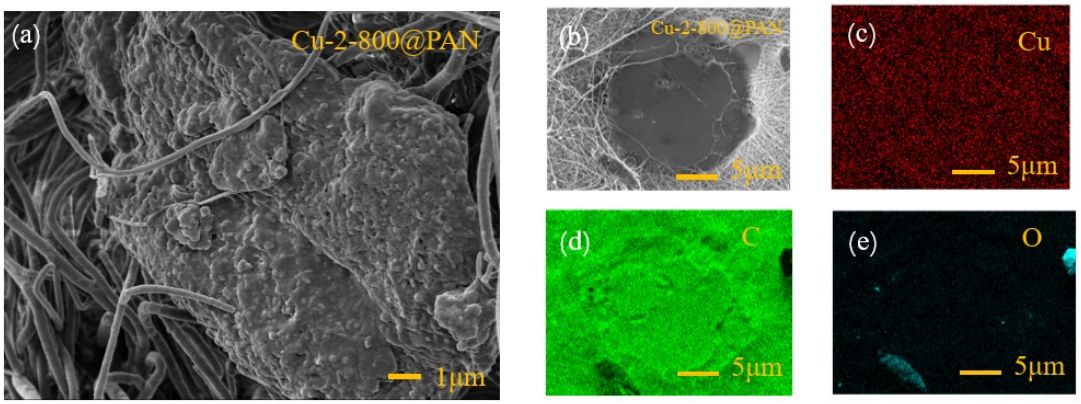

Fig. S13 (a) SEM image of **Cu-2-800@PAN**. (b–e) EDX images of **Cu-2-800@PAN**.

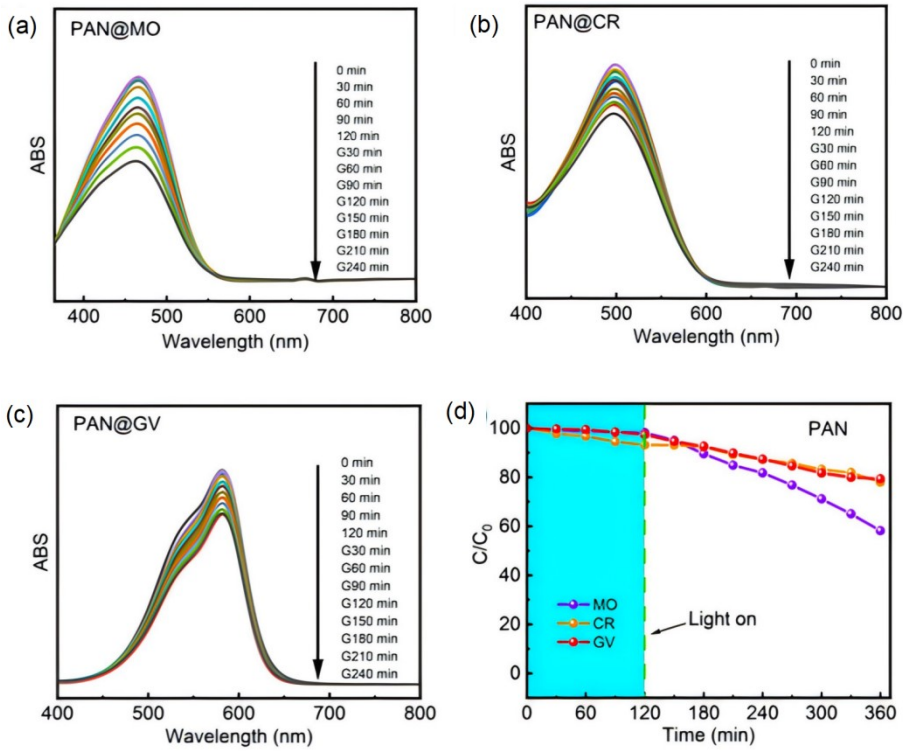

Fig. S14 UV–vis spectra of MO (a), CR (b), and GV (c) solutions which were recorded after photocatalytic degradation had been performed for different lengths of time with original PAN materials. (d) The photodegradation rates of MO, CR, and GV at different time points during exposure to original PAN materials.

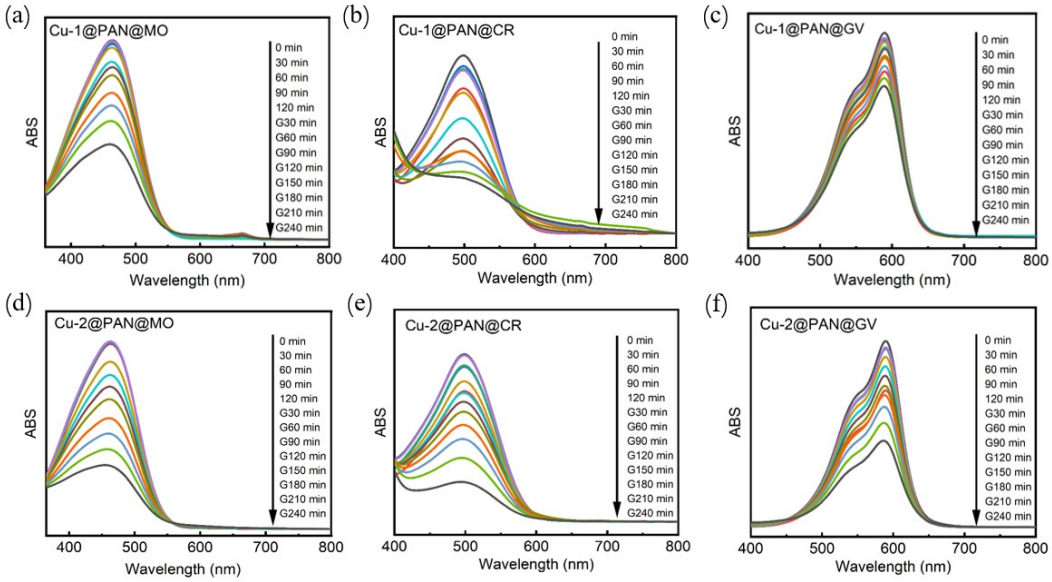

Fig. S15 UV-vis spectra of MO (a), CR (b) and GV (c) solutions recorded after different degradation times with **Cu-1@PAN**. UV-vis spectra of MO (d), CR (e) and GV (f) solutions recorded after different degradation times with **Cu-2@PAN**.

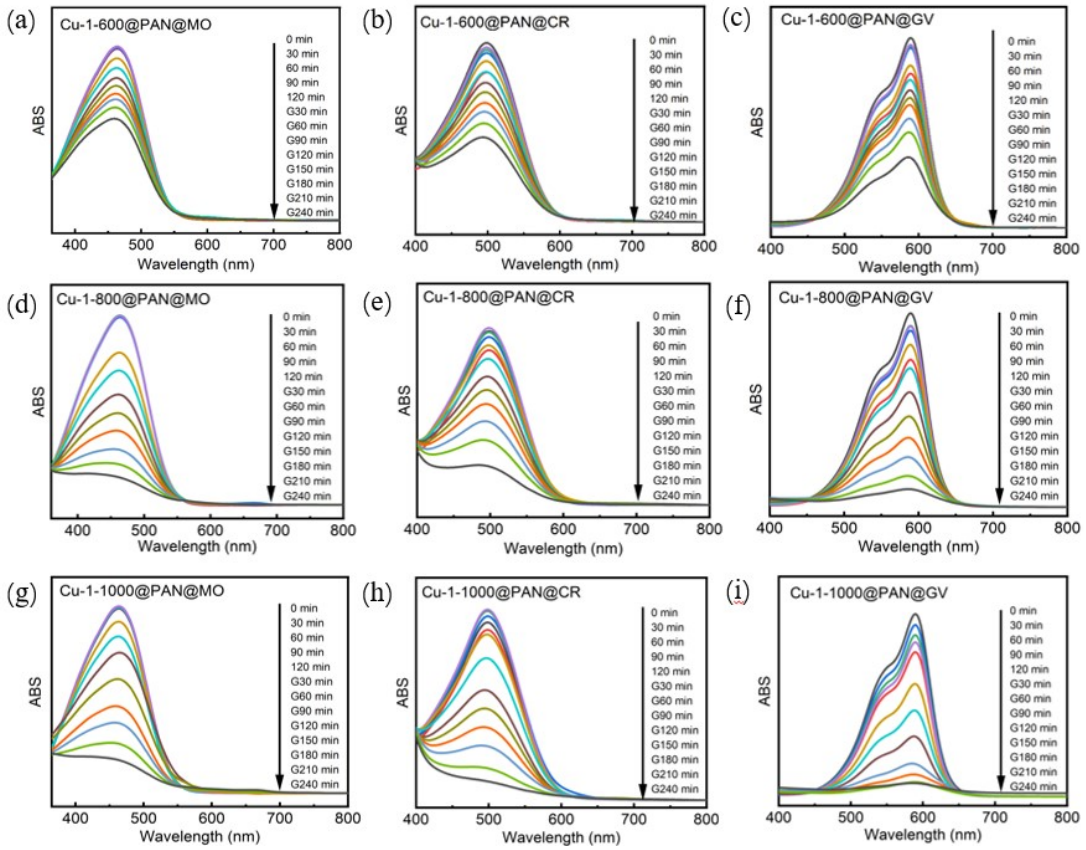

Fig. S16 UV-vis spectra of MO (a), CR (b) and GV (c) solutions recorded after different degradation times with **Cu-1-600@PAN**. UV-vis spectra of MO (d), CR (e) and GV. (f) solutions recorded after different degradation times with **Cu-1-800@PAN**. UV-vis spectra of MO (g), CR (h) and GV. (i) solutions recorded after different degradation times with **Cu-1-1000@PAN**.

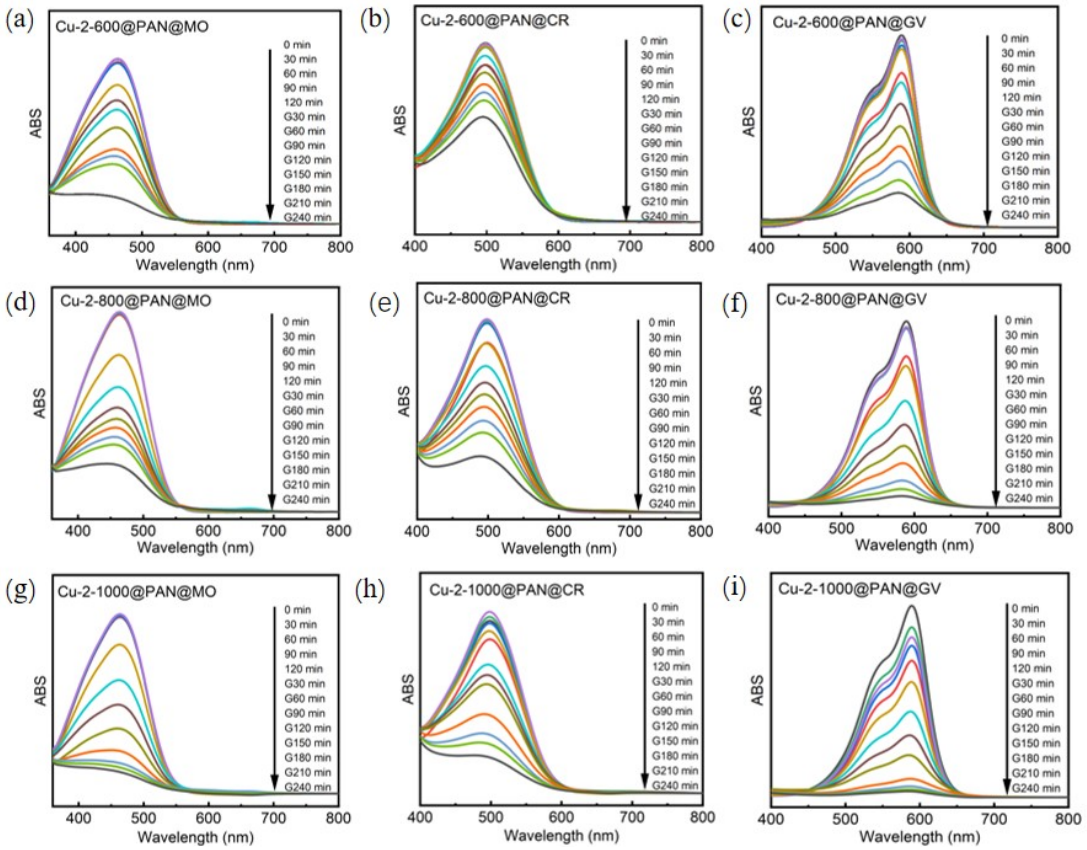

Fig. S17 UV-vis spectra of MO (a), CR (b) and GV (c) solutions recorded after different degradation times with **Cu-2-600@PAN**. UV-vis spectra of MO (d), CR (e) and GV. (f) solutions recorded after different degradation times with **Cu-2-800@PAN**. UV-vis spectra of MO (g), CR (h) and GV. (i) solutions recorded after different degradation times with **Cu-2-1000@PAN**.

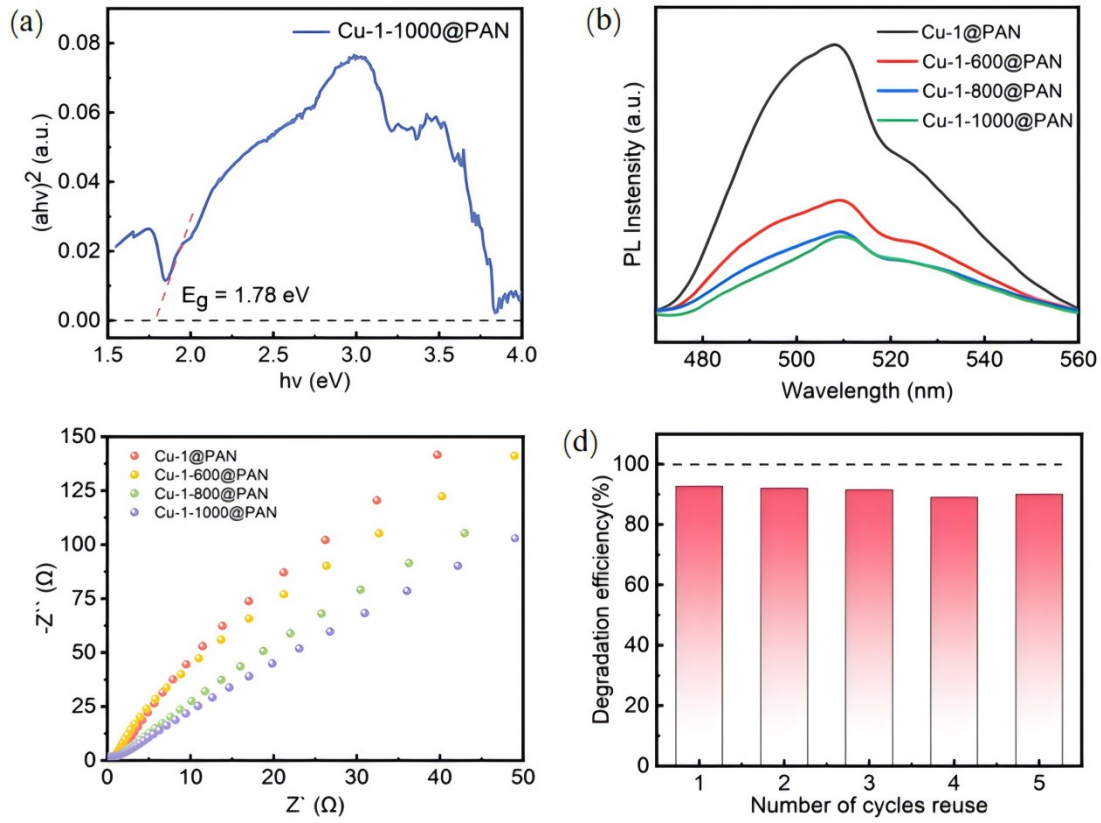

Fig. S18 (a) Band gap of **Cu-1-1000@PAN**. (b) Fluorescence emission spectra of **Cu-1@PAN** and **Cu-1-X@PAN**. (c) Impedance of **Cu-1@PAN** and **Cu-1-X@PAN**. (d) Cyclic stability of **Cu-1-1000@PAN**.

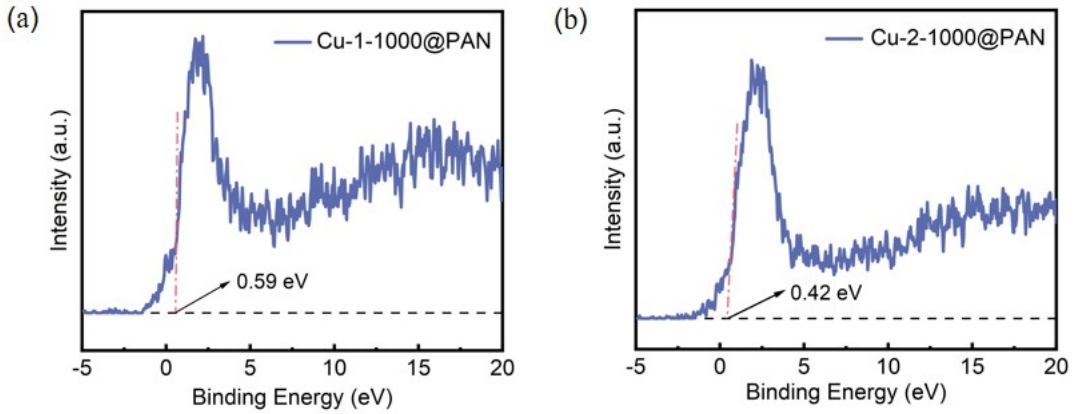

Fig. S19 VB XPS spectra of **Cu-1-1000@PAN** (a) and **Cu-2-1000@PAN** (b).

Supporting Information

Reference

S1 X. L. Wang, J. Luan, H. Y. Lin, C. Xu, G. C. Liu, J. W. Zhang and A. X. Tian, *CrystEngComm*, 2013, **15**, 9995–10006.

S2 G. M. Sheldrick, *Acta Crystallogr. Sect. A*, 2008, **64**, 112–122.